

Article

Deep-Sea Sediment and Water Simulator for Investigation of Methane Seeping and Hydrate Formation

Yan Xie ^{1,2}, Jingchun Feng ^{1,2,*}, Weiqiang Hu ^{1,2}, Mingrui Zhang ^{1,2}, Junwen Wang ^{1,2}, Bo Peng ³, Yujun Wang ³, Zhenwu Zhou ^{1,2} and Yi Wang ^{4,5} 

¹ Southern Marine Science and Engineering, Guangdong Laboratory (Guangzhou), Guangzhou 511458, China; yanxie@gdut.edu.cn (Y.X.); 2112124041@mail2.gdut.edu.cn (W.H.); 2112024030@mail2.gdut.edu.cn (M.Z.); 2112124014@mail2.gdut.edu.cn (J.W.); 2112124025@mail2.gdut.edu.cn (Z.Z.)

² Research Centre of Ecology & Environment for Coastal Area and Deep Sea, Guangdong University of Technology, Guangzhou 510006, China

³ Guangdong Eco-Engineering Polytechnic, Guangzhou 510520, China; pengbo@gig.ac.cn (B.P.); 13711421161@126.com (Y.W.)

⁴ Key Laboratory of Gas Hydrate, Guangzhou Institute of Energy Conversion, Chinese Academy of Sciences, Guangzhou 510640, China; wangyi@ms.giec.ac.cn

⁵ Guangzhou Center for Gas Hydrate Research, Chinese Academy of Sciences, Guangzhou 510640, China

* Correspondence: fengjc@gdut.edu.cn; Fax: +86-020-39322141

Abstract: The ubiquitous methane seeping process in the deep-sea environment could significantly influence the global methane cycle and carbon budget. Hydrate formation on the methane bubble during the seeping process is an important way for sequestering methane during bubble migration. Uncovering the complete methane leakage process needs to reveal the methane leakage pathway and hydrate conversion mechanism. Hence, we built a deep-sea sediment and water simulator to investigate the methane seeping and hydrate formation. The simulator can mimic the deep-sea sediment and water environment with a lower sediment chamber and an upper seawater chamber. The monitoring of the bubble migration path and hydrate transformation and aggregation in the sediment chamber is realized mainly through the spatial distribution of electric resistance and temperature variations. The seawater chamber is equipped with a built-in movable camera and four external windows to observe the rising and morphological evolution of gas and hydrate bubbles. The quantitative storage and escape of CH₄ gas could be realized through the measurement of multiple gas/liquid collection ports and cumulative incoming/outgoing gas volume. In addition, a movable biological liquid injection port was designed in the seawater chamber for the coupling CH₄ conversion of hydrate formation and microorganism-mediated oxidation. Through the experimental test on each function of the system, the effectiveness of the device was proved. The development of this device has pioneering significance for the experimental simulation of the methane seeping process in a simulated submarine cold spring area.

Keywords: methane seeping; hydrate formation; cold seep; simulator



Citation: Xie, Y.; Feng, J.; Hu, W.; Zhang, M.; Wang, J.; Peng, B.; Wang, Y.; Zhou, Z.; Wang, Y. Deep-Sea Sediment and Water Simulator for Investigation of Methane Seeping and Hydrate Formation. *J. Mar. Sci. Eng.* **2022**, *10*, 514. <https://doi.org/10.3390/jmse10040514>

Academic Editor: Timothy S. Collett

Received: 6 March 2022

Accepted: 2 April 2022

Published: 7 April 2022

Publisher's Note: MDPI stays neutral with regard to jurisdictional claims in published maps and institutional affiliations.



Copyright: © 2022 by the authors. Licensee MDPI, Basel, Switzerland. This article is an open access article distributed under the terms and conditions of the Creative Commons Attribution (CC BY) license (<https://creativecommons.org/licenses/by/4.0/>).

1. Introduction

Natural gas hydrate (NGH) is a non-stoichiometric crystalline compound composed of hydrogen-bonded water molecules and gas molecules [1]. NGHs are mainly distributed in the global marine sediment, with the main gas component being CH₄, and 1 m³ of NGH can store about 160–170 m³ of CH₄ gas. The total CH₄ reserve in global NGHs is estimated at approximately 3 × 10¹⁵ m³ (STP), and therefore, NGH was regarded as the largest source of hydrocarbon on the Earth [2]. Due to the characteristics of worldwide distribution, huge reserves, and no pollution after combustion, the effective utilization of NGHs could be conducive to the global transformation to a low-carbon energy system. However, since NGH remains stable only at low temperature and high-pressure conditions, meeting its

thermodynamic stability, the huge CH₄ reserve is also a double-edged sword in the modern world with accelerated global warming [3].

As one of the most important methane reservoirs on earth, NGH plays an important role in methane budget balance and global carbon cycle [4]. However, the rise of marine temperature, geological movement and the NGH exploitation all may lead to the hydrate dissociation and CH₄ leakage [5,6]. Due to the huge reserves of NGHs and their consolidation on sediment particles, only a small amount of dissociation of NGH may lead to a series of environmental problems, such as geological damage, seawater acidification, and biological extinction [7,8]. In addition, the greenhouse effect intensity of CH₄ is 28 times that of CO₂, which has been the second largest greenhouse gas in the world [9]. A large amount of CH₄ released from the seabed may enter the atmosphere, exacerbate global warming, and further result in a vicious cycle of NGH dissociation. Several studies have shown that multiple instances of global warming in historical periods may be related to the large-scale dissociation of NGH [10].

Cold seep, commonly occurring in the NGH stability domain, is a geological phenomenon in which methane-rich fluid migrates from the seabed sediment interface to the water column, and may even reach the atmosphere [11,12]. The discovery of the cold seep provides evidence for the seabed methane leakage. The spilled CH₄ gas in cold seep is commonly derived from dissociated NGH, while generally, the gas does not directly enter the water column or atmosphere. During the migration process, CH₄ could be bio-transformed by aerobic and anaerobic micro-organisms [13]. In addition, a hydrate shell may form at the gas–liquid interface of the rising methane bubbles, which will change their movement characteristics and the dissolution rate of CH₄ into seawater [14]. Moreover, the hydrate formed in submarine sediment may gradually accumulate to form a trap, and this realizes the physical storage of leaked CH₄ gas [15].

The studies on the methane seeping and hydrate transformation characteristics in the cold seep area is of great significance to reveal the methane fate and global carbon budget. However, the current research on seabed CH₄ seeping is mainly based on in situ investigation, such as the seabed ROV observation [16,17] and the in situ Raman measurement [18]. The methane seeping characteristics in the seabed sediments are difficult to obtain, and the time and space for their monitoring are limited. In addition, hardly any experimental studies simultaneously involving methane seeping and hydrate formation behavior of a simulated cold seep environment was reported. In some relative studies, Li et al. [19] investigated the hydrate film formation on a suspended gas bubble and reported that the heat transfer characteristic of hydrate film led to the difference of their morphology. Zeng et al. [20,21] found that gas transportation in the hydrate film thickening process on bubbles experienced a transition from gas pore to lattice. The experiment results of Xie et al. [22] showed that the gas phase composition influences the tightness of the hydrate film on gas bubbles and their mass transfer performance. Li et al. [23] carried out three-dimensional CH₄ hydrate accumulation experiments. The results showed that the temperature field, concentration field, and velocity distribution had a direct impact on the hydrate aggregation and evolution. Experiments examining massive hydrate accumulation in porous sediment by CH₄ gas bubbles were conducted by Madden et al. [24]. They found that bubble pathways and accumulation points controlled the location and characteristics of hydrate deposits, while the research on methane seeping behavior in a simulated seawater environment was lacking in their work. Therefore, it is urgent to study the methane seeping and migration, and the response and transformation of the CH₄ hydrate in a cold seeping environment.

This work describes a newly built deep-sea sediment and water simulator. The device allows the simulation of the migration, transformation, and vertical transmission of leaking CH₄ bubbles in a cold seep environment. By utilizing the spatially distributed temperature and electric resistance measuring points embedded in the simulated submarine sediment, the bubble migration path and the hydrate transformation and aggregation sites in the sediment could be deduced. Flow and morphological characteristics of CH₄ gas and

hydrate bubbles in simulated seawater environments could be directly observed through an inbuilt removable camera and four external windows. Through the regulation of the inlet flow and the measurement of the outlet flow, the experimental simulation of varied CH_4 leakage rates and the capacity calculation of sequestered CH_4 could be realized. The variation law of CH_4 concentration in a simulated seawater layer and gas phase could be obtained by a chromatographic test and quantitative analysis of the samples. In addition, a mobile liquid-injection port was designed for the coupling effect study of hydrate formation and biological oxidation on deep-sea CH_4 seeping in later experiments. In order to validate the good function of each system of the device, a group of experiments was carried out.

2. Apparatus and Methods

2.1. Apparatus Description

This set of experimental systems is mainly composed of Deep-Sea Sediment and Water Simulator (DSSWS) and its corresponding control system. Furthermore, the DSSWS is composed of a simulated overlying seawater chamber and a marine sediment chamber, with the maximum simulated water depth up to 2000 m. The control system mainly includes temperature, pressure, and gas flow. The whole experimental system is presented in Figure 1.

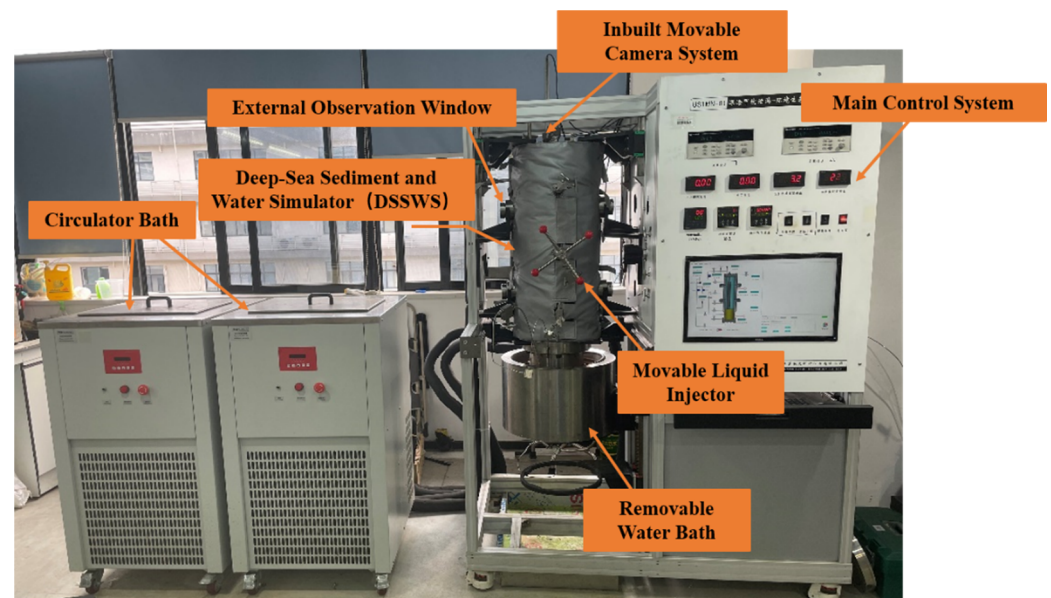


Figure 1. Physical diagram of the experimental system.

2.1.1. Deep-Sea Sediment and Water Simulator (DSSWS)

The material used for building the DSSWS reactor body is 316L stainless steel with corrosion resistance. The DSSWS consists of a lower sediment chamber (LSC) and an upper seawater chamber (USC) connected through threads. The maximum pressure bearing of the DSSWS is 20 MPa. The inner diameters for both of the two chambers are 20 cm and the total height of the DSSWS is 100 cm. The height of LSC and USC are 24.8 cm and 75.2 cm, respectively. The front and section views of the DSSWS are shown in Figure 2a,b, respectively. The measurement equipment in the DSSWS include spatially distributed temperature and electric resistance points, built-in removable camera, external visual windows, and liquid-gas sampling port.

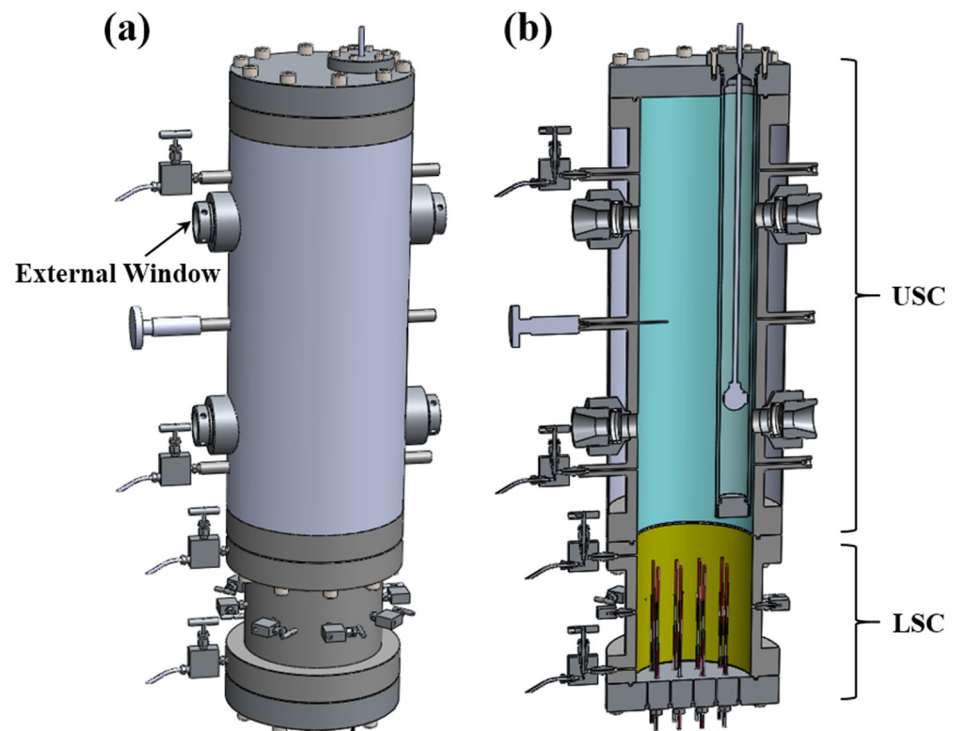


Figure 2. (a) Front and (b) section views of the DSSWS.

The detailed structure of the LSC is shown in Figure 3, which is composed of the connected reactor body and bottom plate (Figure 3c,d). A pair of 4×4 electric resistance transducers were inserted into the lower chamber from the bottom plate. There are three measuring points in the longitudinal direction of each pair of electric resistance transducers, and the height of the corresponding points for all the transducers are the same. Therefore, the chamber contains three layers of electric resistance with 16 electric resistance measurement points in each layer, and the interlayer distance is 6 cm. The total number of electric resistance points in the LSC is 48. The spatial distribution pattern of the temperature measurement points in the sediment simulation chamber is similar to that of the electric resistance, while they are cross distributed with electric resistances on the chamber. There are 13 pairs of temperature transducers with 39 temperature measurement points. Since the inside of the sediment is invisible, the migration path of CH_4 bubbles and hydrate formation sites are reflected mainly through the spatially distributed temperature and electric resistance measurement points. When CH_4 bubble passes or hydrate forms between the electric resistance electrodes, the resistance value will rise. Simultaneously, due to the exothermic effect of hydrate formation, the phase transition area could be monitored by the spatial temperature points. The LSC body is connected with many external valves (Figure 3a,b), which are mainly used for multi-point injection of CH_4 gas. In addition, a pipeline is inserted from the bottom of the plate for the CH_4 gas entry from the bottom of the sediment. Multiple gas inlets can realize the simulation of several gas channels from natural cracks existing in the real sediment environment. The influence of the number of channels on CH_4 seeping could be also investigated. Moreover, the premature end of the simulation experiment caused by hydrate blockage could be avoided through designing multiple gas inlets. Two sampling ports are set on the side wall of the sediment chamber for monitoring and analyzing the liquid components.

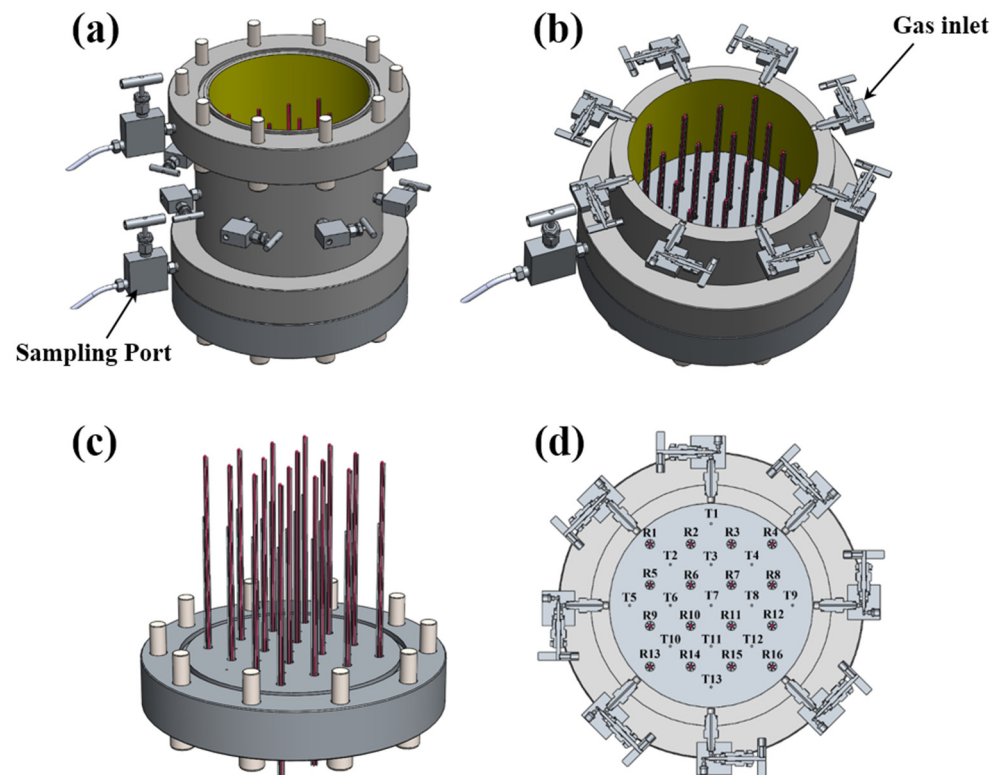


Figure 3. Detailed structure diagram of the LSC. (a) Overall structure, (b) cross-section of LSC body, (c) bottom plate, and (d) top view of temperature and electric resistance layout section.

The USC is mainly used to observe the size, morphology, and vertical motion characteristics of rising CH_4 gas bubbles and CH_4 hydrate bubbles, as well as the CH_4 concentrations in the gas and water phase. The main measurement means including visualization and gas/liquid sampling analysis. Because the motion state of the bubbles may be varied at different heights during its rising process, a built-in movable camera was designed, which allows observation of almost the whole USC. The structure of the built-in movable camera system is shown in Figure 4. It is actually an independent chamber placed in the USC, with a total length of 60 cm and an inner cavity diameter of 6.2 cm. Two high-pressure quartz windows are embedded in the camera chamber. The reason why we did not design a continuous window is that although the viewing field could be further expanded, the required thickness of the window will be significantly increased, resulting in the further reduction of the inner space of the chamber. This is not conducive to the installation of the camera. In this system, the outer wall of the camera system in the seawater simulation chamber is under pressure, while the interior of the chamber is atmospheric pressure connected with the atmosphere. The camera is fixed at the bottom of a movable lever, as shown in Figure 3c, and the other end of the rod is connected with an external motor to realize the movement of the camera. The height and width of the camera field are 7.6 cm and 10.0 cm, respectively.

The physical diagram of the external observation window of the USC is shown in Figure 5, in which the diameter of the window is 3 cm. The water phase state and phenomenon change could be observed directly. There are two windows on both sides of the simulation chamber, one of which is mainly used to provide light source for the chamber. On the same side, two windows are located at the upper and lower parts of the USC, respectively. During the experiment, the bottom windows could be completely immersed in the seawater, and the upper windows are located at the gas–liquid interface. The rising processes of CH_4 bubbles and hydrate, and their state after reaching the interface, can be observed through the bottom and upper windows respectively.

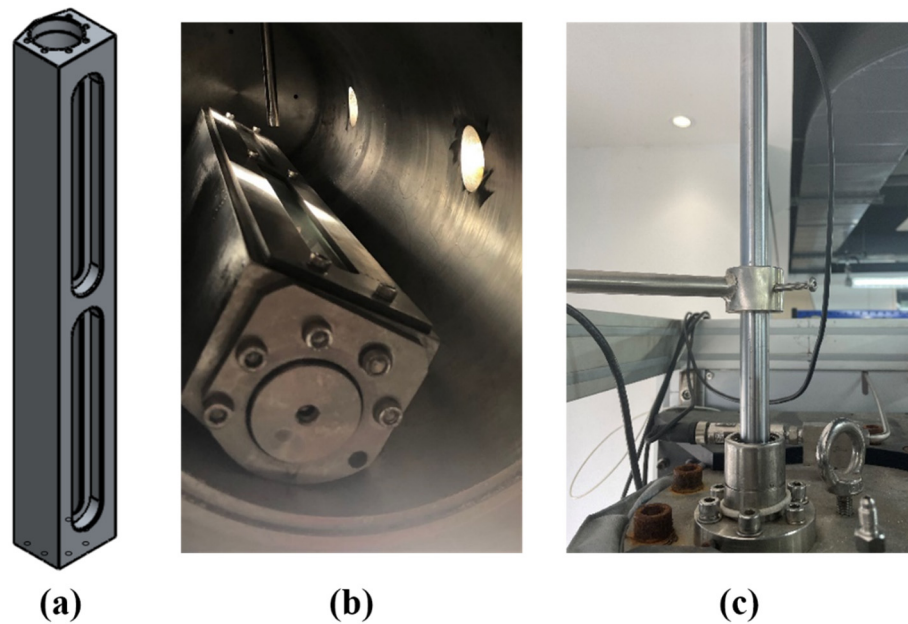


Figure 4. Structure of the built-in movable camera system. (a) Three-dimensional model drawing, (b) physical drawing, and (c) movable lever connected with the camera.



Figure 5. Physical diagram of the external observation window for the seawater simulation chamber.

The USC is equipped with two gas sampling ports and two liquid sampling ports. For the gas collection, one is the continuously flowing gas discharged after flowing through the outlet flowmeter, and the other is the gas gathered from the port located above the seawater simulation chamber, as shown in Figure 6a. The average value of gas components obtained from the two ports is regarded as the actual gas-phase concentration in the top of the USC, and the CH_4 in the gas phase is deemed to escape from the simulated ocean system. Seawater could be collected through the two liquid collecting ports, and the corresponding water sampler is shown in Figure 6b. The main function of this component is to obtain the dissolved CH_4 content in the water at different locations away from the sediment, and to analyze the dissolution and diffusion rate of dissolved CH_4 and its relationship with the spatial location.

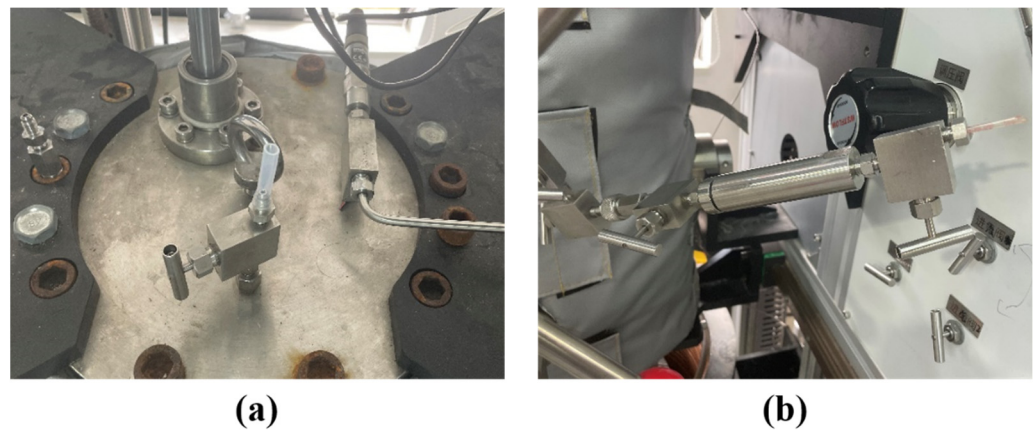


Figure 6. Schematic diagram of (a) the top gas sampling port, and (b) the liquid sampling port with its corresponding water sampler.

In order to simulate the coupling carbon sequestration between micro-organism-mediated methane oxidation and hydrate formation in future experiments, a movable liquid injector was specially designed, as shown in Figure 7a. The liquid containing micro-organisms needs to be injected into the DSSWS under a low temperature and high-pressure condition, which is the reason why we cannot directly add them into the reactor before the experiment. In the process of microbial liquid injection, the injector mainly plays the function of sample injection at different positions in the transverse direction of the USC. The movement back and forth of the injection pipe of the injector is mainly realized by a manual controller. The cross-section of the injector is shown in Figure 7b. In this experimental test, the injector was used as the upper liquid sample port since the CH_4 methane oxidation behaviors mediated by micro-organisms were not studied.

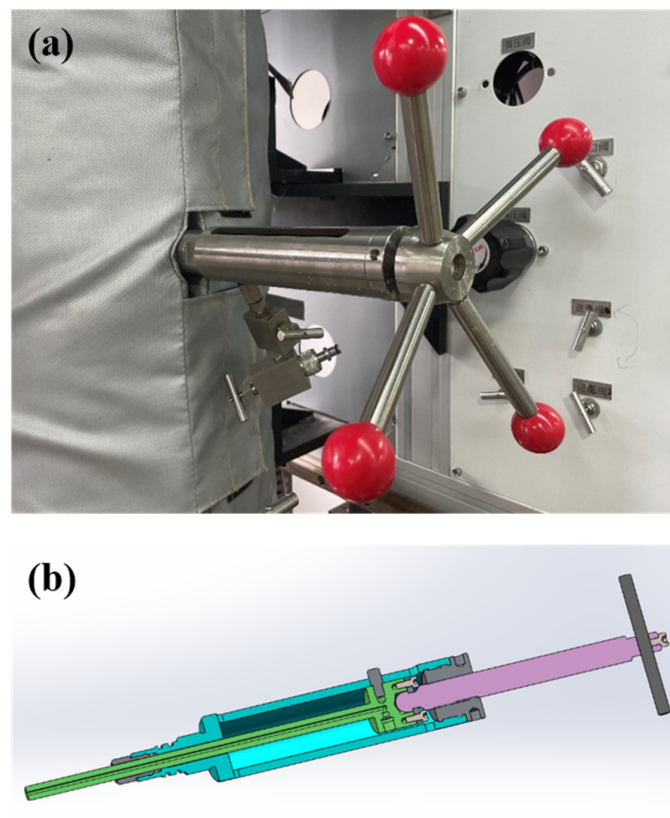


Figure 7. (a) Physical drawing and (b) three-dimensional section of movable liquid injector.

2.1.2. Temperature, Gas Flow, and Pressure Control System

The temperatures of the USC and the LSC are independently controlled by two sets of constant temperature water baths, which makes it possible to realize the temperature gradient distribution as a natural in situ environment [25,26]. The operating temperature range of the two water baths is 263.15 K to 353.15 K. A water jacket is installed on the outer wall of the USC, the frozen liquid circulates in the jacket, and the system temperature is controlled through the heat conduction of the wall. For the LSC, the whole reactor body is submerged in a water bath as shown in Figure 8. The sealing between the LSC and the water bath is realized by an O-ring. The external coolant liquid enters the copper coil surrounded by the inner wall of the water bath, and the coil re-cools the coolant liquid in the water bath. To enhance the temperature uniformity and refrigeration intensity of the coolant liquid in the coil water bath, the liquid was circulated in the bath by using an external power device.



Figure 8. Schematic diagram of the temperature control water bath for the LSC.

The simulated methane seeping rate is controlled by flow controllers, which can record the cumulative CH_4 gas flow at the same time. In this system, two flow controllers are equipped, which can be used for pressure conditions with an inlet pressure no more than 10 MPa and 20 MPa, respectively. The maximum gas flow of both controllers is 1 L/min and the minimum flow rate is 0.01 L/min. The gas output from the reactor is recorded by a gas flowmeter, and the methane storage capacity in the simulated marine system can be calculated combining the difference value between the gas entering and leaving the DSSWS. The constant pressure of the reactor system is mainly controlled by a PID (Proportion Integration Differentiation) procedure during whole experimental process. Once the pressure in the DSSWS is higher than the pressure required for the experiment, the PID valve will be opened for gas exhausting until the system pressure returns to the target pressure. The amount of discharged gas is recorded by the gas flowmeter described above.

The complete experimental system composed of the above parts is shown in Figure 9. A pressure sensor is connected to the inlet and outlet of the reactor, respectively, which is mainly used to judge whether the CH_4 inlet of the sediment simulation chamber is blocked. When the gas inlet pipe is seriously blocked by formed methane hydrate, the inlet pressure of the reactor will gradually be higher than the outlet pressure, which can generally be used as a sign of the end of the experiment. To prove the good functions of the device, a CH_4 seeping experiment was carried out.

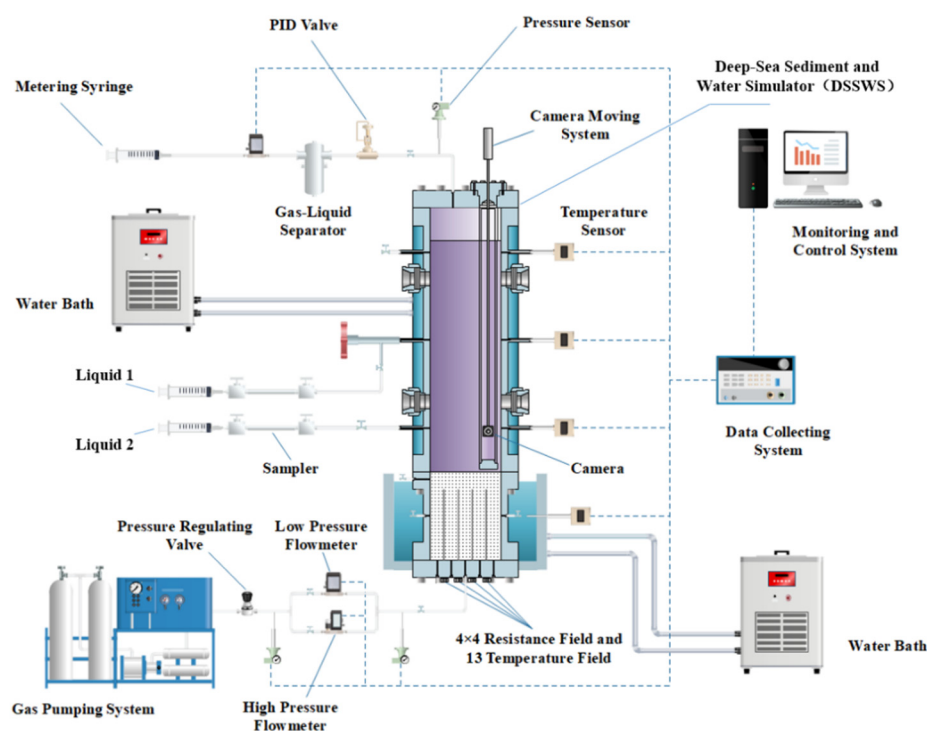


Figure 9. Schematic diagram of the experimental system.

3. Experimental Validation for Methane Seeping and Hydrate Formation

3.1. Experimental Methods

The detailed distribution of the electric resistance and temperature measurement points and the configuration of the gas inlets are shown in Figure 10. Before the experiment, the DSSWS was cleaned with deionized water. Then quartz sand with the particle size of 300–560 μm was filled into the sediment simulation chamber and compacted. The sand was purchased from Yifeng Co., Hebei, China. The actual density of the sand is 2.63 g/cm^3 , with the SiO_2 content being 99.9%. The porosity of the quartz sand sediment is approximately 42%. It should be noted that most marine sediments are mainly clay mixtures with high undrained shear strength and low permeability [27,28], which are the focus of our future research. After the sand was loaded, the USC and LSC were connected and vacuumed. Then, a certain volume of deionized water was injected into the DSSWS through a liquid injection pump to make the liquid level close to flooding the upper windows. Following, the whole system was cooled and stabilized at 277.15 K. After that, N_2 was injected from the top of the USC to pressurize the system to 14 MPa. The reason why N_2 was used instead of CH_4 is that if CH_4 initially existed in the reaction system, the measurement of dissolved CH_4 in simulated seawater will be influenced. Moreover, the existence of CH_4 may lead to the formation of CH_4 hydrate at the gas–liquid interface early. After the system pressure was stable for more than 12 h, the CH_4 gas seeping experiment could be conducted. Before CH_4 gas was pumped, the pressure at the front end of the reactor inlet was slightly greater than 14 MPa to prevent liquid backflow. In this experiment, the gas flow rate was 200 mL/min, and a total of six gas inlets were used, including the bottom inlet of the sediment simulation chamber. The detail of the inlets' configuration is shown in Figure 10. When the gas inlets were opened, the temperature and electric resistance in the sediment simulation chamber started recording. The recording position of the internal camera was periodically moved to obtain bubble motion information at different heights. In addition, the collection of the gas phase and simulated seawater, and the analysis of their gas components, need to be carried out termly during the experiment. The visual state change from the external windows was monitored. The specific parameters of various sensors used in this study are listed in Table 1.

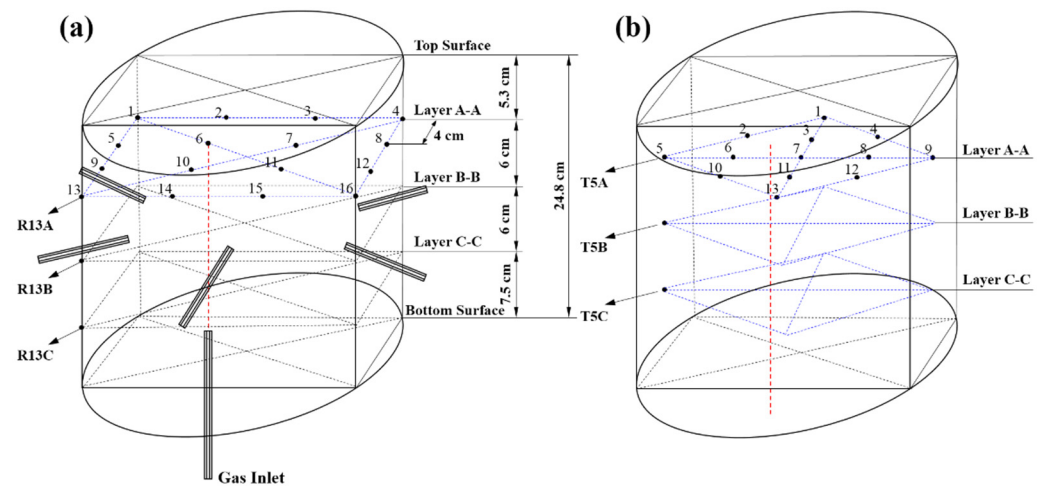


Figure 10. (a) Electric resistance, (b) temperature measurement points distribution, and gas inlet configurations in the DSSWS.

Table 1. Summary of the specific parameters of the various sensors.

Number	Sensor Type	Test Ranges	Accuracy
1	Temperature	−20~280 °C	±0.1 °C
2	Pressure	0~25,000 KPa	±25 KPa
3	Electric resistance	0~1000 KΩ	±0.1 KΩ

3.2. Experimental Results

3.2.1. Electric Resistance and Temperature Evolution Characteristics

The evolution of R_t/R_0 ratios for R10 and R13 in the three layers during the whole CH_4 seeping process is shown in Figure 11. The R_0 represents the initial resistance value before CH_4 gas entered, and R_t represents the resistance value at time t . In the initial CH_4 seeping stage, the resistance values hardly change until about 2.58 h; the three values of R13 began to increase significantly. This can be mainly attributed to the growth of CH_4 hydrate around them [29,30]. The increased rates of R13B and R13C were faster than that of R13A in the first 0.3 h after the resistance values rose, while after the first 0.5 h, R13A soared linearly. After about 10 h of the experiment, the rapid increase in R13 resistance values ended and the value presented as $A > C > B$ at this time. Following, the resistance value of R13 rose slowly between 10~110 h, which may be because the formed hydrate hindered the migration of methane gas. The changed resistance value in this process could be mainly contributed to the slow development in hydrate saturation with the increased hydrate formation limitation. At about 115 h, the resistance value of R13 fluctuated significantly, and then continued to increase. This phenomenon may be attributed to hydrate morphology change and gas disturbance. In comparison, the multiples of the raised resistance values in R13 were significantly greater than those in R10. Each the resistance value of R10 did not rise until around 32 h.

The space distributions of electric resistances in the simulated marine sediment from the starting point to the end point of methane seeping is shown in Figure 12. In the first 20 h of the experiment, only the electric resistance for R13 increased significantly, while the resistance value of other positions in the space remained almost unchanged. The electric resistance at other positions increased slightly at 41.7 h, in which the increment of R1 was the most obvious. At 120 h, the resistance value in the whole sediment increased visibly, indicating that CH_4 hydrate had been distributed in the whole sediment space. It can be found from the spatial electric resistance distribution at 146.7 h that the most obvious increase of resistance value occurred at the edge of sediment. It indicated that the gas leakage channels were easier to form at the edge, which may be related to the

lower shear strength and correspondingly higher permeability of the sediments [27,28]. In addition, the electric resistance of R13 showed a trend of continuous rise throughout the experimental period.

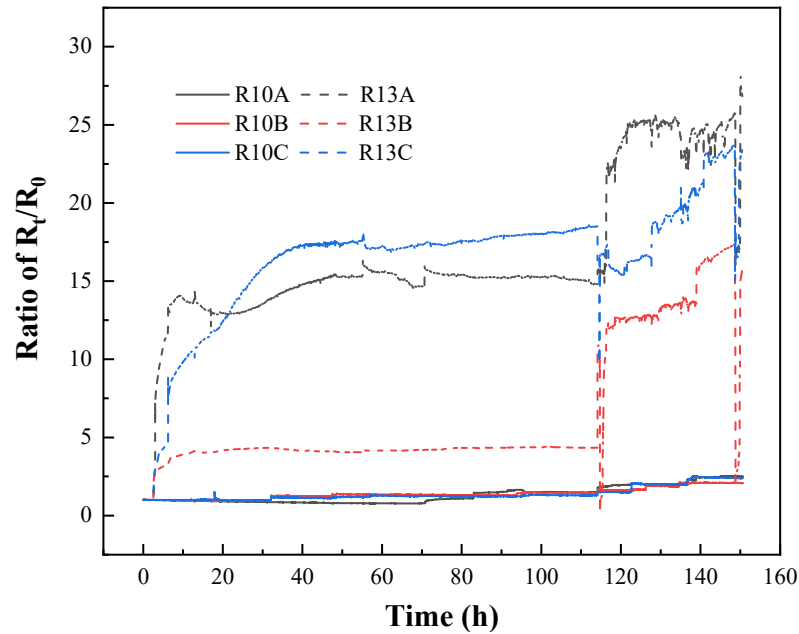


Figure 11. Electric resistance changes of R10 and R13 in the three layers during CH₄ gas seeping.

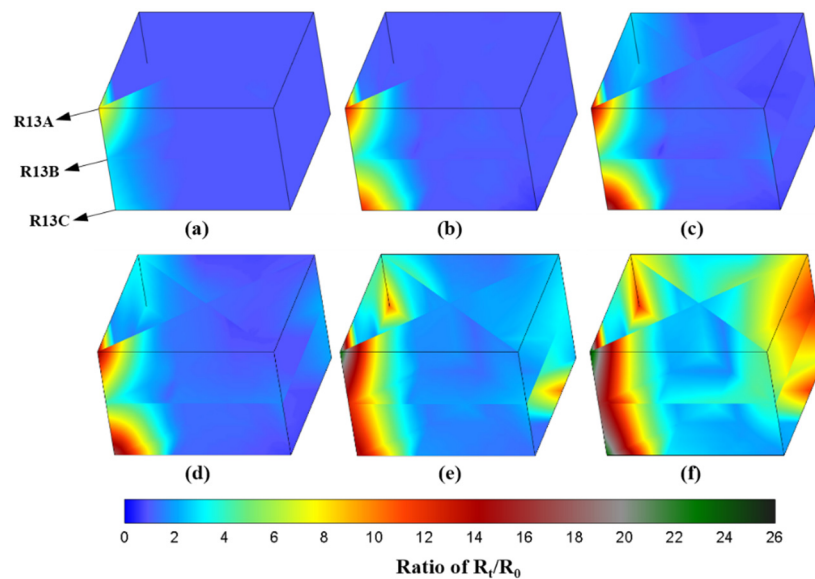


Figure 12. Space distributions of electric resistances in the simulated marine sediment from the starting point to the end point of methane seeping. (a) 3.3 h, (b) 20 h, (c) 41.7 h, (d) 83.3 h, (e) 120 h, (f) 146.7 h.

The spatial distribution of temperatures in sediment is illustrated in Figure 13. In this experiment, there was no obvious local temperature rise in the sediment caused by hydrate formation [31–34]. Only the spatial temperature distributions at two time points are presented here. This implied that there was no massive accumulation of CH₄ gas bubbles during the initial hydrate nucleation and formation processes. Consequently, the heat release from the hydrate formation by single or few CH₄ bubbles was not enough to change the local temperature in a water-saturated environment. In the whole experimental process, the temperature of each point in the sediment was maintained around 277.15 K.

However, there was a gradually increasing temperature gradient from the bottom to top, as seen in Figure 13. This is because of the direct contact between the top of the coolant liquid with the air, which will be further improved in the next experiment.

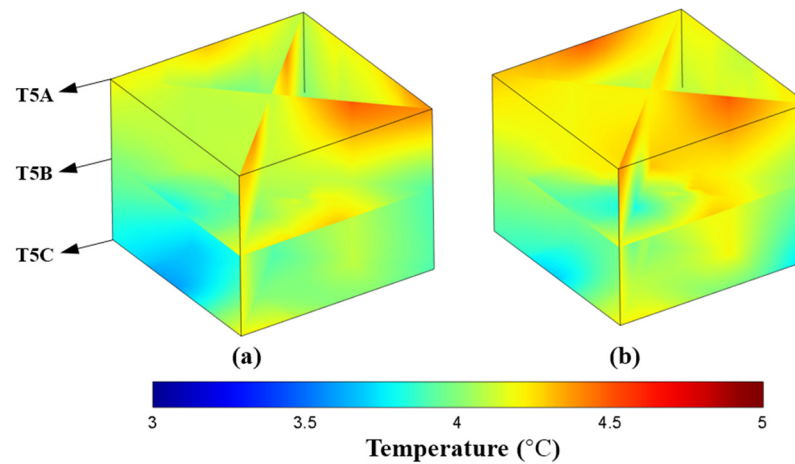


Figure 13. Space distributions of temperatures in the simulated marine sediment from the starting point to the end point of methane seeping. (a) 3.3 h, (b) 83.3 h.

3.2.2. Gas Content Change in the Liquid and Gas Phases

Figure 14 presents the changes of CH₄ and N₂ proportions of dissolved gas in the liquid phase and free gas in the gas phase during the experiment. The ratio of CH₄-to-N₂ can be obtained directly by gas chromatography measurement. It can be found that in the first 120 h, the proportion changes of CH₄ and N₂ in the lower water phase, upper water phase, and gas phase had high consistency, and there was no obvious difference in the content. After 120 h, the proportion of CH₄ in the gas phase was gradually greater than that in the liquid phase, and the CH₄ proportion in the upper liquid phase was higher than that in the lower liquid phase. The detail content change of dissolved gas in unit water in the upper and lower liquid phases is shown in Figure 15. The calculation method of dissolved gas content in unit volume water is shown in Equation (1). In the time span of the experiment, the dissolved CH₄ content in the upper and lower parts of the solution both gradually increased with the methane seeping progress. The change trend of the dissolved CH₄ content in the two parts was the same before 120 h, and the CH₄ content was almost the same. However, after 120 h, the content of CH₄ in the upper aqueous phase was greater than that in the lower aqueous phase, which was constant with the CH₄ and N₂ proportion change in Figure 14. In the whole experimental process, the dissolved methane in the water phase gradually increased, which was partly due to the dissolution of leakage of methane gas. In addition, some CH₄ hydrates dissociated, and the generated methane dissolved in the aqueous phase. During the 100~150 h range, the declined dissolved methane content, especially the concentration at the liquid 2 sampling port, was related to the formation of CH₄ hydrate by dissolved gas. This may also be one of the reasons why the R13 resistance values increased obviously again around 120 h, as shown in Figure 11. For the dissolved N₂, the content in the upper aqueous phase had a slight rise in the whole experiment, and the content in the lower aqueous phase gradually increased until it became relatively stable after 100 h.

$$S_a = \frac{V_g \times C_a}{V_w} \tag{1}$$

where S_a represents the dissolved gas “a” content in unit volume of water. V_g represents the total gas volume in the sampled liquid. C_a is the proportion of gas “a” in the total gas, which was directly measured by gas chromatography. V_w represents the total volume of the sampled liquid.

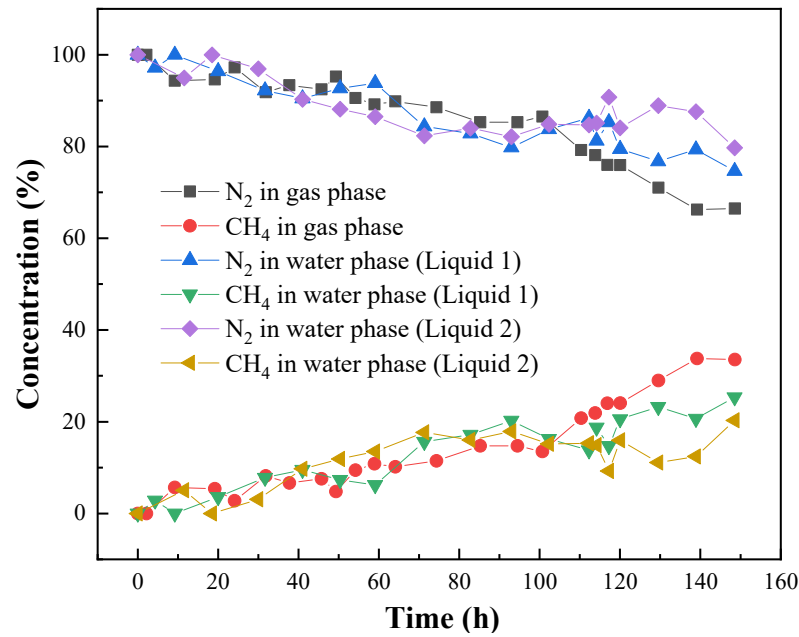


Figure 14. Changes of CH₄ and N₂ proportions of dissolved gas in the liquid phase and free gas in the gas phase during the whole experiment.

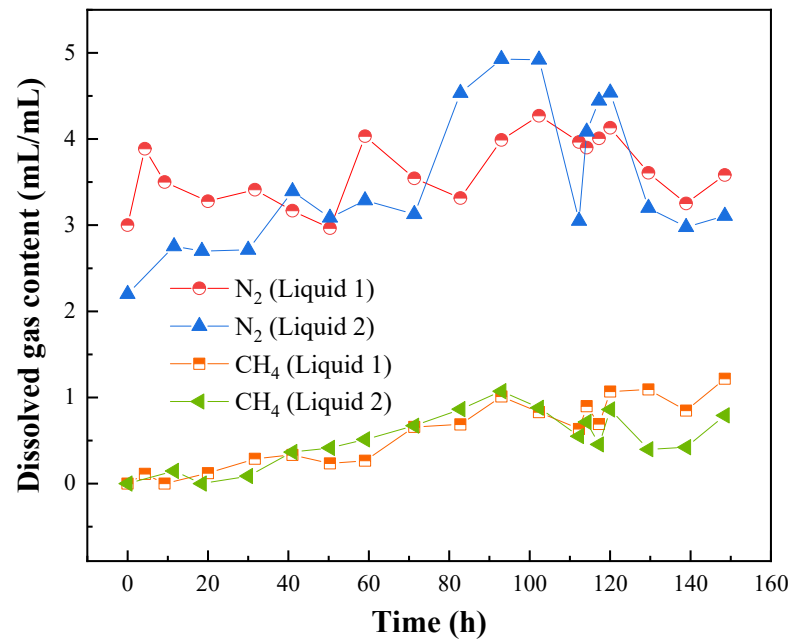


Figure 15. Dissolved gas content change in unit water in the upper and lower liquid phases.

3.2.3. Cumulative Volume Changes of Incoming and Outgoing Gas

The cumulative incoming CH₄ gas and outgoing CH₄/N₂ gas during the experiment are shown in Figure 16. It can be found that the entered gas was greater than the exhaust in the whole experimental process, and the difference value gradually rose, indicating that an increased amount of CH₄ gas was captured and stored in the simulated marine system. However, in the whole experimental process, the cumulative gas volume of the outlet kept increasing, indicating that the gas was constantly leaking out of the system. The leaked CH₄, dissolved gas storage, free gas storage, and hydrate storage can be calculated by combining the changes of CH₄/N₂ content in the two phases of gas and liquid in Figures 14 and 15 and the changes of cumulative gas flows in Figure 16.

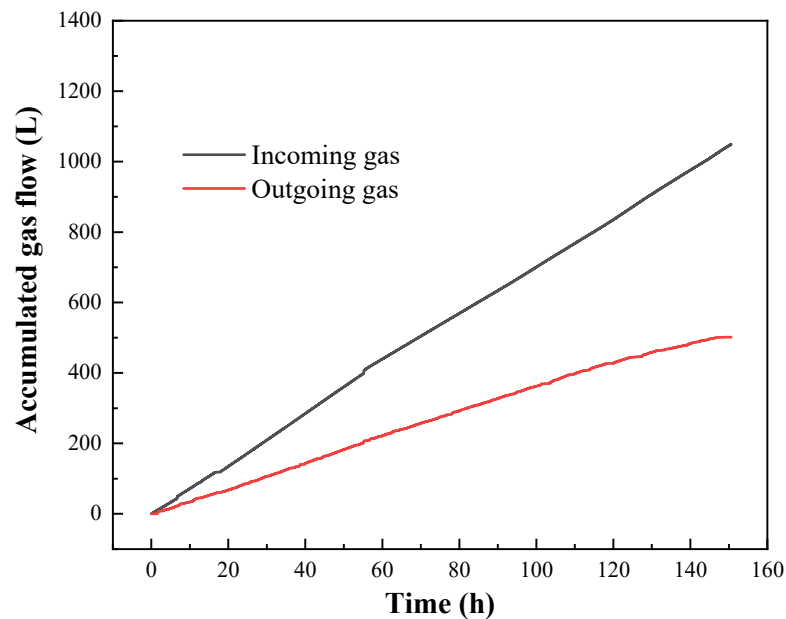


Figure 16. Cumulative incoming CH_4 gas and outgoing CH_4/N_2 gas changes during the experiment.

3.2.4. Visual Observation with Built-In Camera and External Windows

Figure 17 illustrates several phenomena in the USC at different times and positions recorded by the built-in camera, including the rising of CH_4 gas bubbles and hydrate bubbles, the floating of hydrate particles, the formation of flocculent hydrate, and the accumulation of hydrate bubbles. A large number of small-sized bubbles seeped out of the sediment almost at the same time as shown in Figure 17b. This might be due to local gas binding in the sediment until it erupted suddenly. Since the methane leaked from the sediment to the simulated seawater was mainly in the form of gas bubbles, the hydrates shown in Figure 17c–e were mainly formed by dissolved methane. Due to the cementation between hydrates, once newly raised bubbles touched the accumulated hydrate bubbles, they were easy to be adhered, as presented in Figure 17f. Consequently, the accumulation scale of strand hydrate bubbles gradually expanded. The influence of hydrate film on bubble motion could be analyzed through the gas bubble size, hydrate bubble size and morphology, and rising speed, etc. Figure 18 presents the change of the gas–liquid interface photographed from the upper window. At around 20 h, the first hydrate bubble was found on the interface, even though hydrate had formed in the sediment within 3 h, as shown in Figure 11. However, due to the harsh N_2 hydrate phase equilibrium conditions [35], the CH_4 hydrate bubble could not keep stability until the gas phase was filled with enough methane gas. The gradual accumulation of hydrate bubbles at the top of the water is similar to the situation in which the rising bubbles are blocked by coke rock in a natural marine environment, which could further enhance the sequestration ability of the ocean for leaked methane.

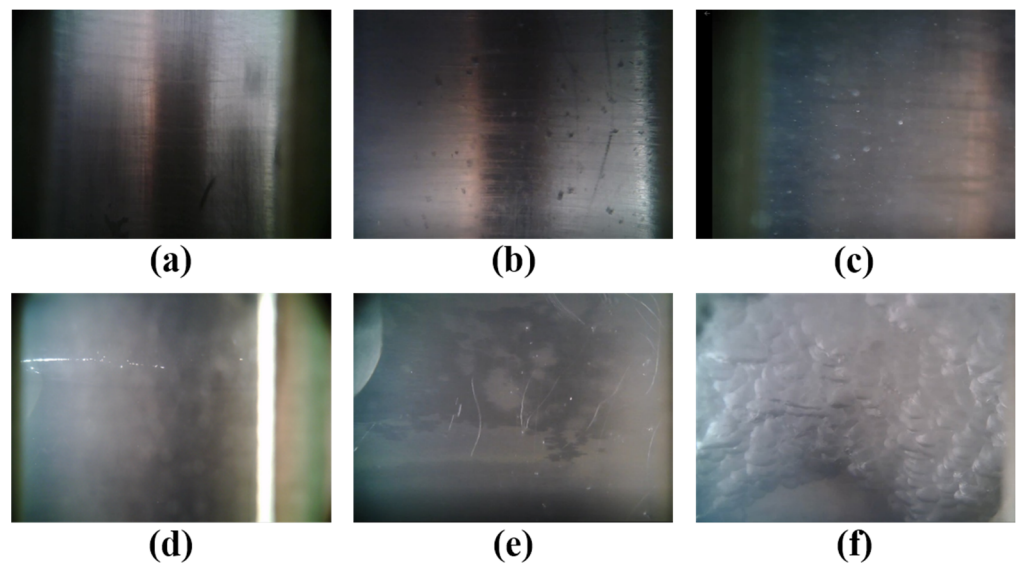


Figure 17. Image recording through built-in camera. (a) View inside the USC before CH₄ seeping experiment; (b) gas bubbles rising rapidly at 1.67 h; (c) CH₄ hydrate particles rising at 22 h; (d) hydrate sheet at 26 h; (e) flocculent hydrate at 37 h; (f) accumulated hydrate bubbles at 100 h.

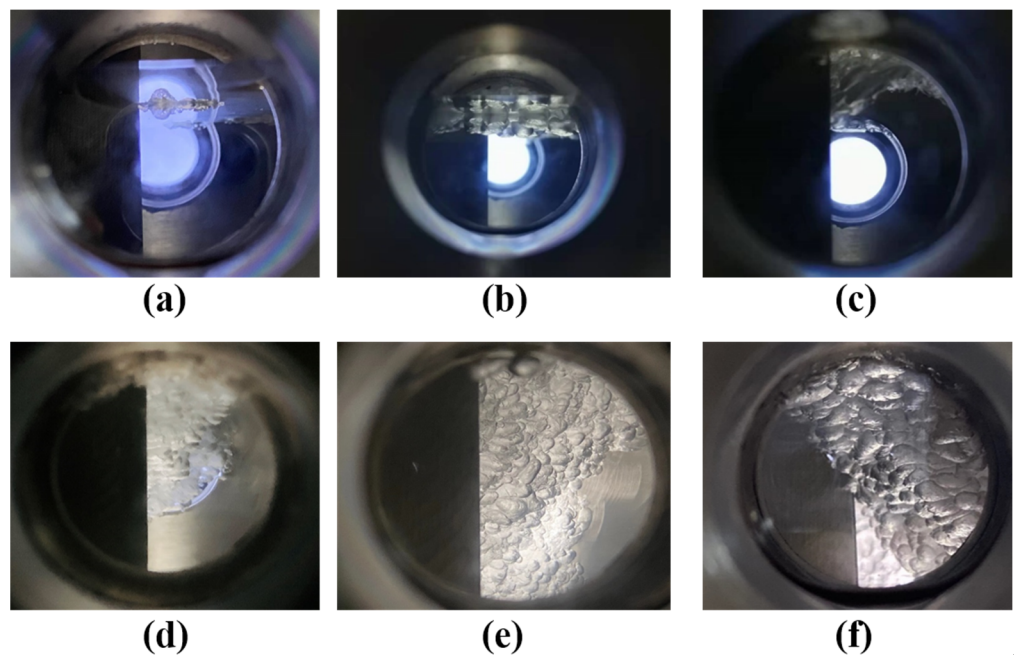


Figure 18. Image recording through the external windows that hydrate the bubbles floating at the gas–liquid interface and their accumulation process at (a) 20 h, (b) 24 h, (c) 64 h, (d) 97 h, (e) 120 h, and (f) 145 h.

4. Conclusions

This work describes a newly built deep-sea division and water simulator. The simulator consists of a lower sediment simulation chamber and an upper seawater simulation chamber, which were developed for the investigation of the methane seeping and hydrate formation.

1. The monitoring of the bubble migration path and hydrate transformation and aggregation in the sediment chamber could be realized, mainly through the spatial distribution of electric resistance and temperature measurement points.

2. The rising characteristic and morphological evolution of gas and hydrate bubbles in seawater chamber are recorded through a built-in, movable camera and four external windows.
3. The quantitative storage and escape of CH₄ could be realized through the measurement of multiple gas/liquid collection ports and cumulative incoming/outgoing gas volumes.
4. The effectiveness test of the experiment system showed that the local sediment resistance values increased first, and after a period of time, the sediment resistance values rose as a whole. Only the accumulative CH₄ bubbles form the hydrate simultaneously, and a large amount of exothermic heat may lead to the obvious change of local temperature. In addition, the image recording and gas measurement results also presented a great regularity. The experimental results prove the good functions of the simulator.

Author Contributions: Conceptualization, J.F. and Y.W. (Yi Wang); methodology, Y.X.; software, M.Z.; validation, Y.X., W.H., M.Z., J.W. and Z.Z.; formal analysis, J.F.; investigation, B.P.; resources, Y.W. (Yujun Wang); data curation, W.H.; writing—original draft preparation, Y.X.; writing—review and editing, J.F.; visualization, Y.W. (Yi Wang); supervision, J.F.; project administration, J.F.; funding acquisition, J.F. All authors have read and agreed to the published version of the manuscript.

Funding: Financial support was received from the National Natural Science Foundation of China (42022046), the National Key Research and Development Program of China (2021YFF0502300), the Key Special Project for Introduced Talents Team of Southern Marine Science and Engineering Guangdong Laboratory (Guangzhou) (GML2019ZD0403 and GML2019ZD0401), and Guangzhou Science and Technology Project (202102020971), and is gratefully acknowledged.

Institutional Review Board Statement: Not applicable.

Informed Consent Statement: Not applicable.

Data Availability Statement: Data associated with this research are available and can be obtained by contacting the corresponding author.

Conflicts of Interest: The authors declare no conflict of interest.

References

1. Sloan, E.D.; Koh, C.A. *Clathrate Hydrates of Natural Gases*, 3rd ed.; CRC Press: Boca Raton, FL, USA, 2008.
2. Boswell, R.; Collett, T.S. Current perspectives on gas hydrate resources. *Energy Environ. Sci.* **2011**, *4*, 1206–1215. [[CrossRef](#)]
3. Masson-Delmotte, V.P.; Zhai, H.O.; Pörtner, D.; Roberts, J.; Skea, P.R.; Shukla, A.; Pirani, W.; Moufouma-Okia, C.; Péan, R. Summary for Policymakers, In *Global Warming of 1.5 °C, An IPCC Special Report on the Impacts of Global Warming of 1.5 °C above Preindustrial Levels and Related Global Greenhouse Gas Emission Pathways, in the Context of Strengthening the Global Response to the Threat of Climate Change, Sustainable Development, and Efforts to Eradicate Poverty*. IPCC, 2018, *in press*.
4. Reeburgh, W.S. Oceanic methane biogeochemistry. *Chem. Rev.* **2007**, *107*, 486–513. [[CrossRef](#)] [[PubMed](#)]
5. Ketzer, M.; Praeg, D.; Rodrigues, L.F.; Augustin, A.; Pivel, M.A.; Rahmati-Abkenar, M.; Miller, D.J.; Viana, A.R.; Cupertino, J.A. Gas hydrate dissociation linked to contemporary ocean warming in the southern hemisphere. *Nat. Commun.* **2020**, *11*, 3788. [[CrossRef](#)] [[PubMed](#)]
6. Rutqvist, J.; Moridis, G.J. Development of a numerical simulator for analyzing the geomechanical performance of hydrate-bearing sediments. In *Proceedings of the 42nd US Rock Mechanics Symposium and 2nd US-Canada Rock Mechanics Symposium San Francisco, Onepetro, San Francisco, CA, USA, 29 June–2 July 2008*.
7. Zhu, C.Q.; Li, Z.H.; Chen, D.X.; Li, S.Z.; Song, X.S.; Shan, H.X.; Jia, Y.G. Seafloor breathing helping forecast hydrate-related geohazards. *Energy Rep.* **2021**, *7*, 8108–8114. [[CrossRef](#)]
8. Van Dover, C.L.; German, C.R.; Speer, K.G.; Parson, L.M.; Vrijenhoek, R.C. Evolution and biogeography of deep-sea vent and seep invertebrates. *Sci. Justice* **2002**, *295*, 1253–1257. [[CrossRef](#)]
9. Pachauri, R.K.; Allen, M.R.; Barros, V.R.; Broome, J.; Cramer, W.; Christ, R.; Church, J.A.; Clarke, L.; Dahe, Q.; Dasgupta, P.; et al. *Climate Change 2014: Synthesis Report. Contribution of Working Groups I, II and III to the Fifth Assessment Report of the Intergovernmental Panel on Climate Change*. IPCC **2014**, *9*, 151.
10. Hinrichs, L.R.; Hmelo, L.R.; Sylva, L.R. Molecular fossil record of elevated methane levels in late Pleistocene coastal waters. *Sci. Justice* **2003**, *299*, 1214–1217. [[CrossRef](#)]
11. Suess, E.; Carson, B.; Ritger, S.D.; Moore, J.C.; Cochrane, G.R. Biological communities at vent sites along the subduction zone off Oregon. *Bull. Biol. Soc. Wash.* **1985**, *6*, 475–484.

12. Paull, C.K.; Dillon, W.P. Natural gas hydrates: Occurrence, distribution, and detection. *Wash. DC Am. Geophys. Union Geophys. Monogr. Ser.* **2001**, *15*, 124.
13. Ruppel, C.D.; Kessler, J.D. The interaction of climate change and methane hydrates. *Rev. Geophys.* **2017**, *55*, 126–168. [[CrossRef](#)]
14. Feng, D.; Qiu, J.W.; Hu, Y.; Peckmann, J.; Guan, H.X.; Tong, H.P.; Chen, C.; Chen, J.X.; Gong, S.G.; Li, N.; et al. Cold seep systems in the South China Sea: An overview. *J. Asian Earth Sci.* **2018**, *168*, 3–16. [[CrossRef](#)]
15. Su, K.H.; Sun, C.Y.; Dandekar, A.; Liu, B.; Sun, W.Z.; Cao, M.C.; Li, N.; Zhong, X.Y.; Guo, X.Q.; Ma, Q.L.; et al. Experimental investigation of hydrate accumulation distribution in gas seeping system using a large scale three-dimensional simulation device. *Chem. Eng. Sci.* **2012**, *82*, 246–259. [[CrossRef](#)]
16. Wei, J.G.; Li, J.W.; Wu, T.T.; Zhang, W.; Li, J.T.; Wang, J.L.; Tao, J.; Chen, Z.H.; Wu, Z.J.; Chen, W.L. Geologically controlled intermittent gas eruption and its impact on bottom water temperature and chemosynthetic communities—A case study in the “HaiMa” cold seeps South China Sea. *Geol. J.* **2020**, *55*, 6066–6078. [[CrossRef](#)]
17. Römer, M.; Sahling, H.; Pape, T.; Bohrmann, G.; Spiess, V. Quantification of gas bubble emissions from submarine hydrocarbon seeps at the Makran continental margin (offshore Pakistan). *J. Geophys. Res. Ocean.* **2012**, *117*, C10015. [[CrossRef](#)]
18. Du, Z.F.; Zhang, X.; Xi, S.C.; Li, L.F.; Luan, Z.D.; Lian, C.; Wang, B.; Yan, J. In situ Raman spectroscopy study of synthetic gas hydrate formed by cold seep flow in the South China Sea. *J. Asian Earth Sci.* **2018**, *168*, 197–206. [[CrossRef](#)]
19. Li, S.L.; Sun, C.Y.; Liu, B.; Li, Z.Y.; Chen, G.J.; Sum, A.K. New observations and insights into the morphology and growth kinetics of hydrate films. *Sci. Rep.* **2014**, *4*, 4129. [[CrossRef](#)]
20. Zeng, X.Y.; Wu, G.Z.; Zhong, J.R.; Chen, D.Y.; Sun, C.Y.; Chen, G.J. Three-Scale in Situ Investigation on the Film Morphology and Mass Transfer Channels during the Thickening Growth of Hydrates on Gas Bubble. *Cryst. Growth Des.* **2019**, *19*, 3158–3165. [[CrossRef](#)]
21. Zeng, X.Y.; Wu, G.; Zhang, S.; Sun, L.; Sun, C.; Chen, G.; Feng, J.C. In-situ Raman study on kinetics behaviors of hydrated bubble in thickening. *Sci. Total Environ.* **2022**, *814*, 152476. [[CrossRef](#)]
22. Xie, Y.; Zheng, T.; Zhu, Y.J.; Zhong, J.R.; Feng, J.C.; Sun, C.Y.; Chen, G.J. Effects of H₂-N₂ on CO₂ hydrate film growth: Morphology and microstructure. *Chem. Eng. J.* **2022**, *431*, 134004. [[CrossRef](#)]
23. Li, N.; Sun, Z.F.; Sun, C.Y.; Li, P.; Chen, G.J.; Ma, Q.L.; Liu, B. Simulating natural hydrate formation and accumulation in sediments from dissolved methane using a large three-dimensional simulator. *Fuel* **2018**, *216*, 612–620. [[CrossRef](#)]
24. Madden, M.E.; Ulrich, S.; Szymcek, P.; McCallum, S.; Phelps, T. Experimental formation of massive hydrate deposits from accumulation of CH₄ gas bubbles within synthetic and natural sediments. *Mar. Pet. Geol.* **2009**, *26*, 369–378. [[CrossRef](#)]
25. Li, X.S.; Xu, C.G.; Zhang, Y.; Ruan, X.K.; Li, G.; Wang, Y. Investigation into gas production from natural gas hydrate: A review. *Appl. Energy* **2016**, *172*, 286–322. [[CrossRef](#)]
26. Xie, Y.; Li, R.; Wang, X.H.; Zheng, T.; Cui, J.L.; Yuan, Q.; Qin, H.B.; Sun, C.Y.; Chen, G.J. Review on the accumulation behavior of natural gas hydrates in porous sediments. *J. Nat. Gas Sci. Eng.* **2020**, *83*, 103520. [[CrossRef](#)]
27. Guo, X.S.; Nian, T.K.; Wang, D.; Gu, Z.D. Evaluation of undrained shear strength of surficial marine clays using ball penetration-based CFD modelling. *Acta Geotech.* **2021**, *16*, 1–17. [[CrossRef](#)]
28. Guo, X.S.; Nian, T.K.; Zhao, W.; Gu, Z.D.; Liu, C.P.; Liu, X.L.; Jia, Y.G. Centrifuge experiment on the penetration test for evaluating undrained strength of deep-sea surface soils. *Int. J. Min. Sci. Technol.* **2021**, *in press*. Available online: <https://www.sciencedirect.com/science/article/pii/S2095268621001476> (accessed on 1 March 2022).
29. Zhao, J.H.; Liu, C.L.; Li, C.F.; Zhang, Y.C.; Bu, Q.T.; Wu, N.Y.; Liu, Y.; Chen, Q. Pore-Scale Investigation of the Electrical Property and Saturation Exponent of Archie’s Law in Hydrate-Bearing Sediments. *J. Mar. Sci. Eng.* **2022**, *10*, 111. [[CrossRef](#)]
30. Zhou, X.T.; Fan, S.S.; Liang, D.Q.; Wang, D.L.; Huang, N.S. Use of Electrical Resistance to Detect the Formation and Decomposition of Methane Hydrate. *J. Nat. Gas Chem.* **2007**, *16*, 399–403. [[CrossRef](#)]
31. Feng, J.C.; Li, B.; Li, X.S.; Wang, Y. Effects of depressurizing rate on methane hydrate dissociation within large-scale experimental simulator. *Appl. Energy* **2021**, *304*, 117750. [[CrossRef](#)]
32. Li, P.; Feng, J.C.; Yang, Z.F.; Zhang, S.; Zeng, X.Y.; Sun, L.W.; Huang, Y.Y.; Zhang, M.; Feng, X.; Yin, H. Kinetic Behaviors of Methane Hydrate Formation with Bubble Seeping at Conditions of “Haima” Cold Seep. *Energy Fuels* **2021**, *35*, 12132–12141. [[CrossRef](#)]
33. Yang, X.; Sun, C.Y.; Su, K.H.; Yuan, Q.; Li, Q.P.; Chen, G.J. A three-dimensional study on the formation and dissociation of methane hydrate in porous sediment by depressurization. *Energy Convers. Manag.* **2012**, *56*, 1–7. [[CrossRef](#)]
34. Xie, Y.; Zheng, T.; Zhong, J.R.; Zhu, Y.-J.; Wang, Y.F.; Zhang, Y.; Li, R.; Yuan, Q.; Sun, C.Y.; Chen, G.J. Experimental research on self-preservation effect of methane hydrate in porous sediments. *Appl. Energy* **2020**, *268*, 115008. [[CrossRef](#)]
35. Arjmandi, M.; Chapoy, A.; Tohidi, B. Equilibrium data of hydrogen, methane, nitrogen, carbon dioxide, and natural gas in semi-clathrate hydrates of tetrabutyl ammonium bromide. *J. Chem. Eng. Data* **2007**, *52*, 2153–2158. [[CrossRef](#)]